

Electronic Supplementary Information

Mesoporous iron oxide directly anchored on graphene matrix for lithium-ion battery anodes with enhanced strain accommodation

Mingbo Zheng,[‡] Danfeng Qiu,[‡] Bin Zhao, Luyao Ma, Xinran Wang, Zixia Lin, Lijia Pan,
Youdou Zheng, and Yi Shi*

*Nanjing National Laboratory of Microstructures, School of Electronic Science and Engineering,
Nanjing University, Nanjing 210093, China.*

Fax: 86-25-83621220; Tel: 86-25-83621220; E-mail: yshi@nju.edu.cn.

[‡] These authors contributed equally to this work.

Experimental

Synthesis of GNS: Graphite oxide (GO) was synthesized from natural graphite powders (universal grade, 99.985%) according to a modified Hummers method. Dried GO was thermally exfoliated at 300 °C for 3 min in air, and then treated at 900 °C for 3 h in Ar at a heating rate of 2 °C/min. The obtained sample was denoted as GNS. The heat-treatment at 900 °C makes the sample possesses excellent electrical conductivity.

Synthesis of MIO/GNS: In a typical synthesis of MIO/GNS nanocomposite, Fe(NO₃)₃·9H₂O (505 mg) was first dissolved in ethanol (35 mL). GNS (50 mg) was added to the solution, and ultrasonication was performed for 10 min. The suspension was magnetically stirred in a ventilation cabinet, and ethanol was evaporated continuously. Afterwards, the sample was collected and treated at 40 °C for 24 h in a blast drying oven. The dried Fe(NO₃)₃·9H₂O/GNS composite was subsequently treated at 200 °C for 10 h in a blast drying oven. The mechanism can be illustrated by the following equation: 4Fe(NO₃)₃·9H₂O → 2Fe₂O₃ + 12NO₂ + 3O₂ + 9H₂O. The final iron oxide content in the MIO/GNS nanocomposite was about 67 wt%.

Synthesis of simplex MIO: Simplex MIO sample was prepared by the heat treatment of Fe(NO₃)₃·9H₂O at 200 °C for 10 h in an blast drying oven.

Synthesis of Fe₃O₄/GNS: For the synthesis of Fe₃O₄/GNS, Fe(NO₃)₃·9H₂O/GNS composite was heat treated at 600 °C for 6 h in Ar. The other processes were identical to those for MIO/GNS. The final Fe₃O₄ content in the MIO/GNS nanocomposite was about 66 wt%.

Characterization: XRD patterns were obtained by a Bruker D8 Advance diffractometer. Mössbauer spectra were obtained in a transmission configuration and in constant acceleration mode at room temperature with a radioactive source of ⁵⁷Co in Rh matrix. The morphologies of the samples were examined by TEM (JEOL, JEM-2100) and SEM (Hitachi S-4800). N₂ adsorption-desorption analysis was performed using a Micromeritics ASAP 2010 instrument. Infrared absorption spectra were collected from 4000–500 cm⁻¹ on a Nicolet-670 FTIR spectrometer. X-ray photoelectron spectroscopy was measured by a PHI5000 VersaProbe spectrometer (ULVAC-PHI).

Lithium-ion battery performance measurement: 80 wt% active material, 10 wt% carbon black, and 10 wt% polyvinylidfluoride binder were mixed with N-methylpyrrolidone. The obtained slurry was coated onto a copper foil current collector and dried in a vacuum. The loading of the tested electrodes in our experiments is 1.0 mg cm⁻² to 1.1 mg cm⁻². Coin half cells were assembled in an argon-filled glove-box using an active material as the working electrode, a Li metal foil as the counter electrode, 1 M LiPF₆ in ethylene carbonate and diethyl carbonate (1:1 vol) as the electrolyte, and Celgard 2250 as the separator. Full cells with commercially available LiMn₂O₄ and LiCoO₂ as the cathodes and the MIO/GNS nanocomposite as the anode were also assembled in the same argon-filled glove-box. The tested cathodes were prepared using similar methods as that of the MIO/GNS slurry. The resultant LiMn₂O₄ and LiCoO₂ slurries were uniformly pasted onto alumina foil and dried in vacuum. The weights of the cathode and anode for the nanocomposite/LiMn₂O₄ full cell were 5.96 and 0.60 mg, respectively. The weights of the cathode and anode for the nanocomposite/LiCoO₂ full cell were 5.35 and 0.61 mg, respectively. Charge-discharge measurements were carried out galvanostatically using a battery testing system (LAND, Wuhan Jinnuo Electronics. Ltd.). Cyclic voltammetry was carried out on a CHI 660C electrochemistry workstation in a two-electrode system.

Figures:

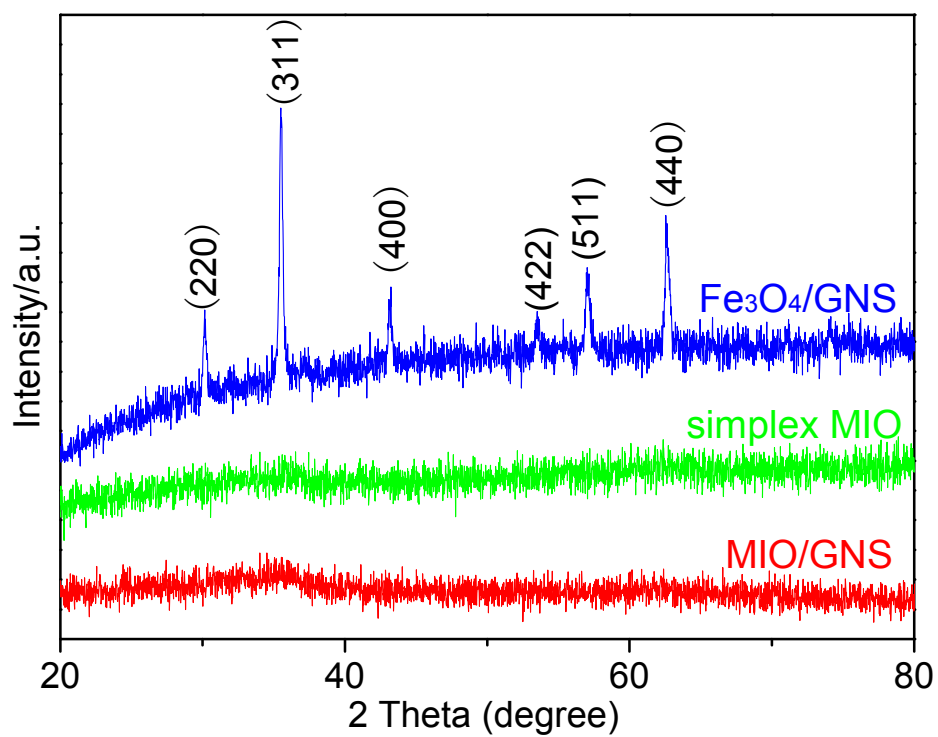


Fig. S1. XRD patterns of MIO/GNS, simplex MIO, and Fe₃O₄/GNS. The characteristic peaks in the pattern of Fe₃O₄/GNS is coincident with the standard profile of magnetite Fe₃O₄ (JCPDS File Card No. 19-0629)

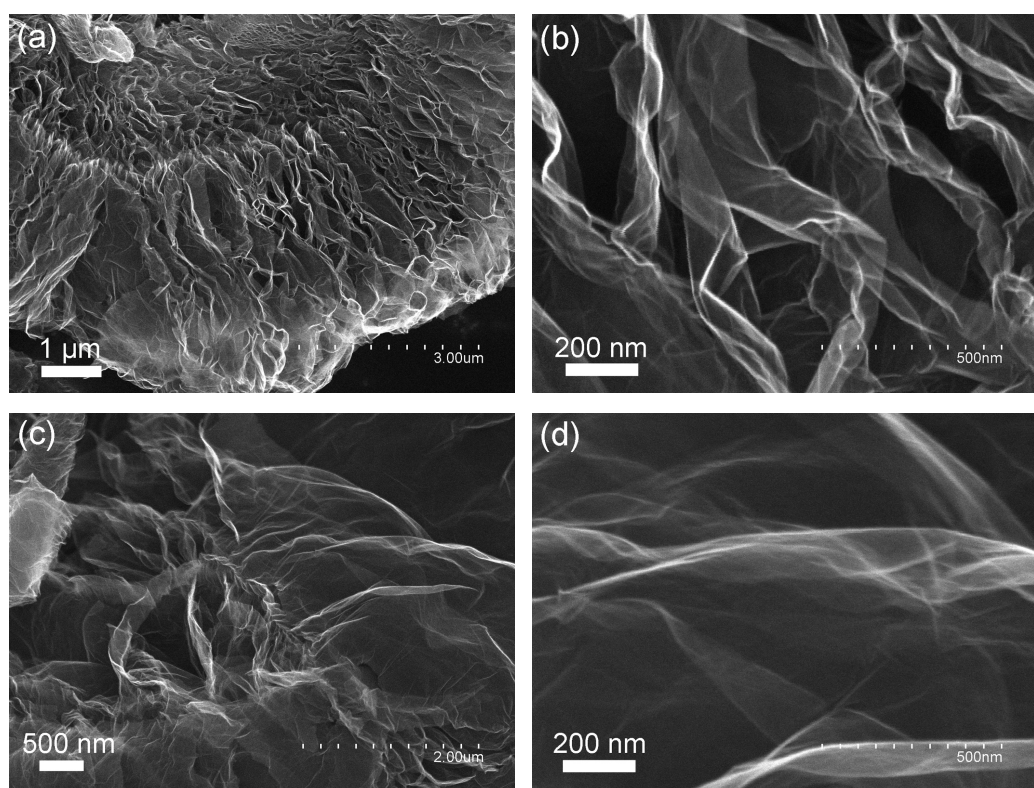


Fig. S2. SEM images of GNS

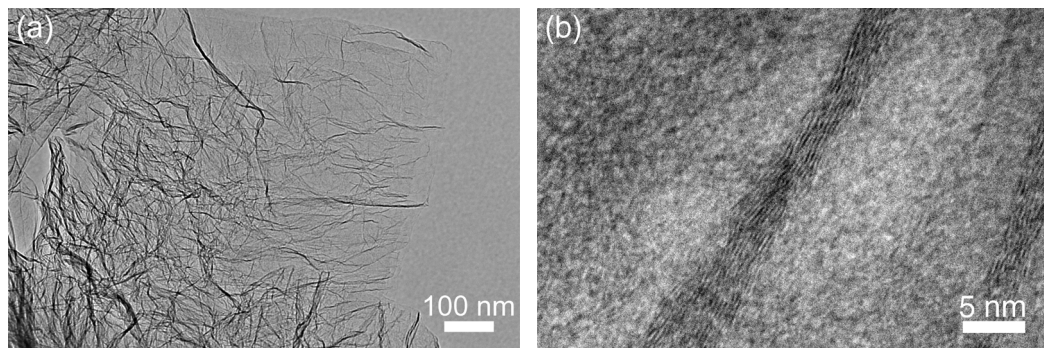


Fig. S3. TEM images of GNS. Figure b shows that the sample is composed of multilayered graphene nanosheets.

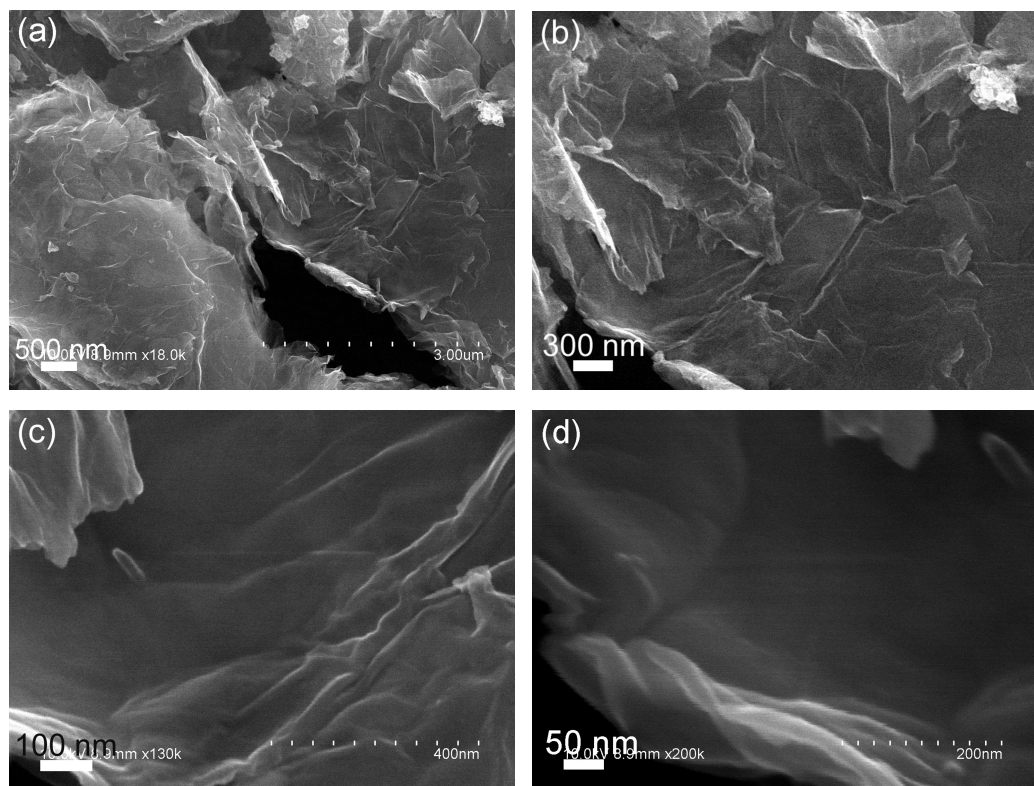


Fig. S4. SEM images of MIO/GNS nanocomposite at different magnifications.

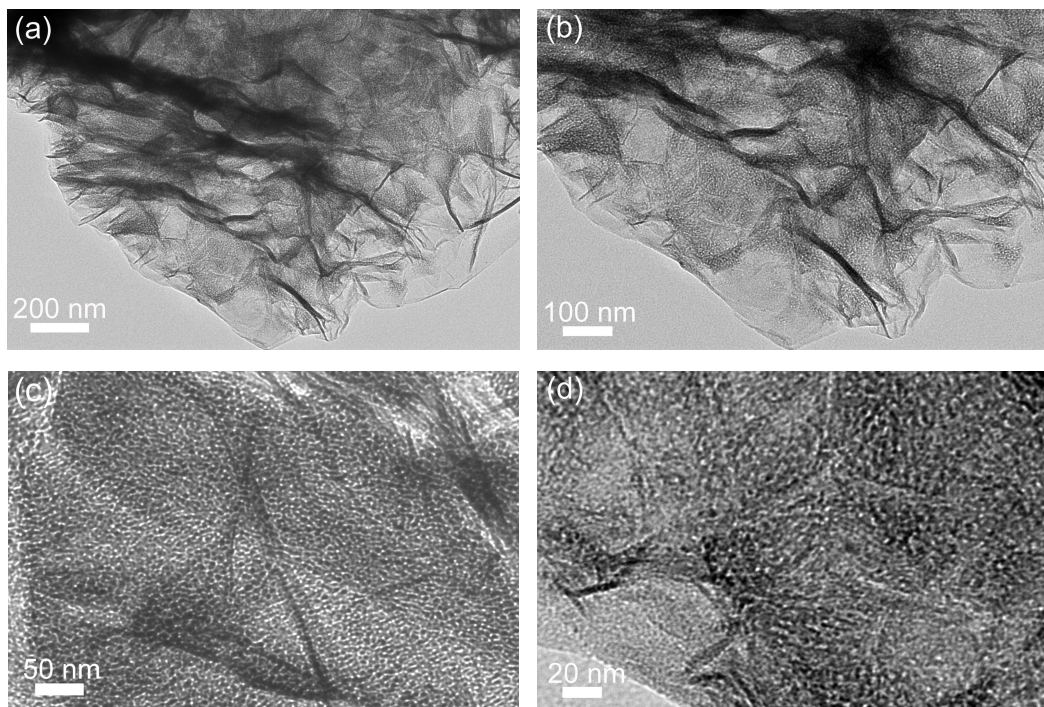


Fig. S5. TEM images of MIO/GNS nanocomposite at different magnifications.

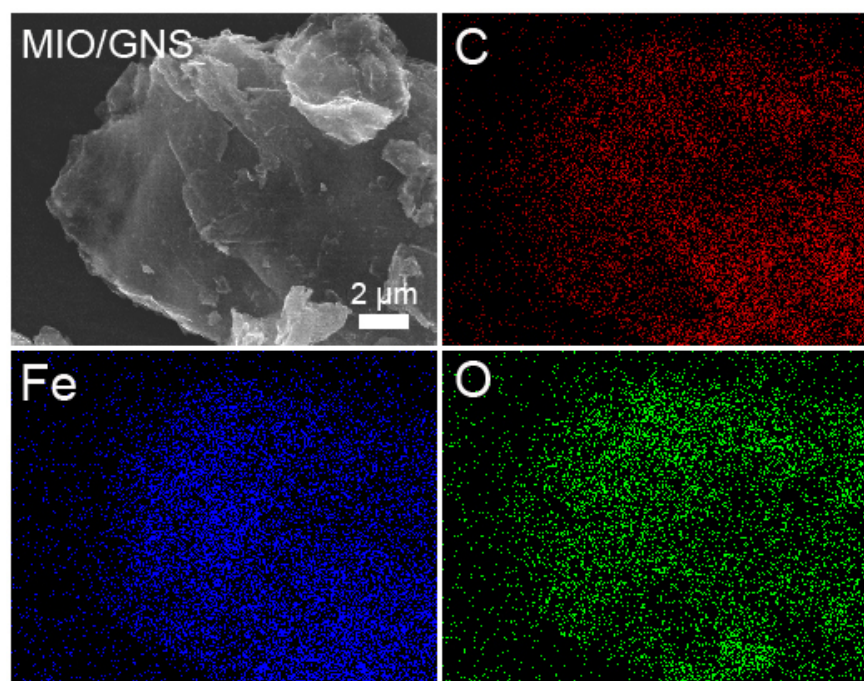


Fig. S6. SEM image and corresponding carbon, iron, and oxygen elemental mapping of MIO/GNS

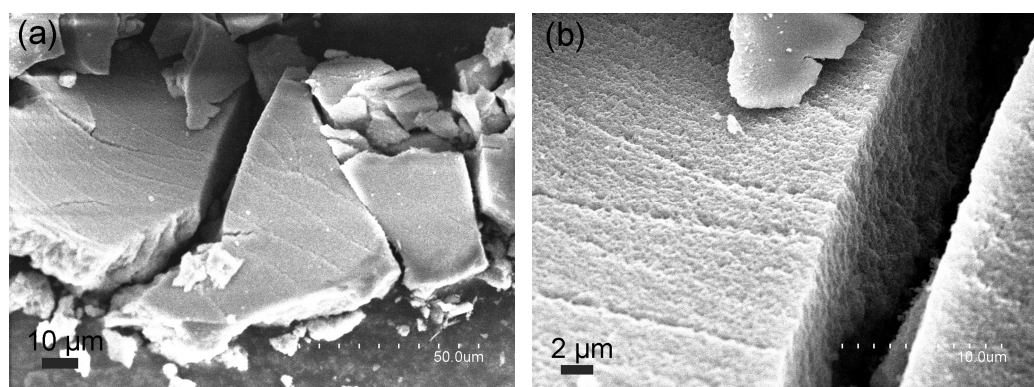


Fig. S7. SEM images of simplex MIO. The sample was composed of very large particles.

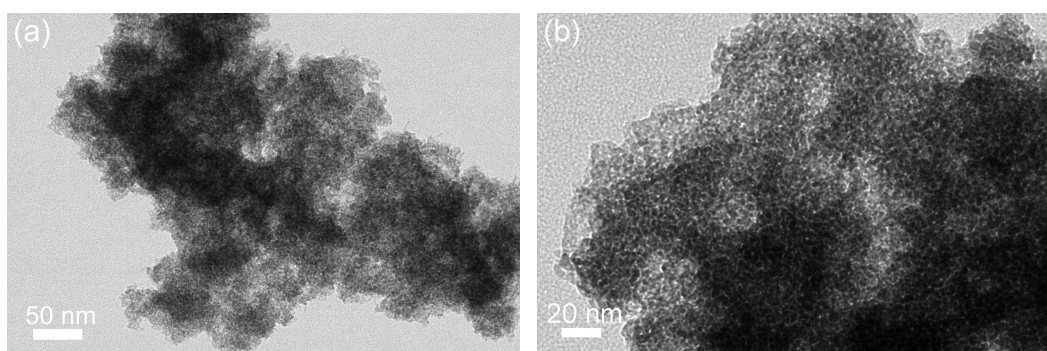


Fig. S8. TEM images of simplex MIO. Before TEM observation, the sample was ground and then treated by ultrasonic for 10 minutes to obtain small particles.

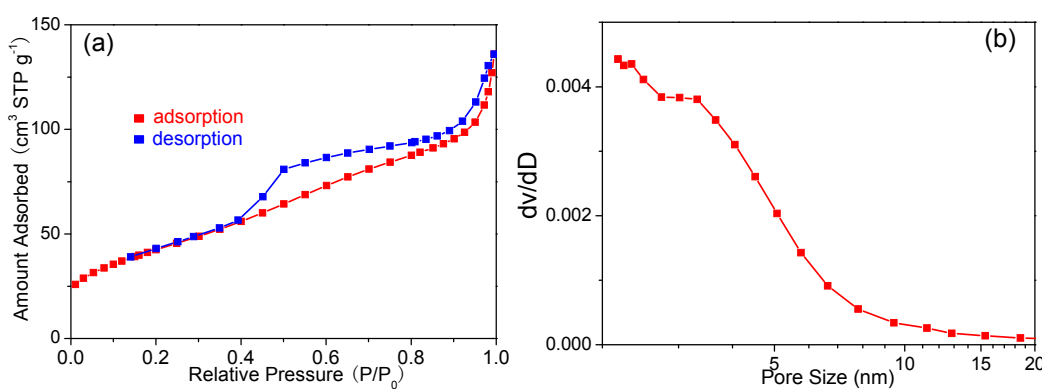


Fig. S9. (a) N₂ adsorption-desorption isotherms and (b) BJH pore size distribution curve from adsorption branch for simplex MIO. The sample possesses a BET surface area of 154 m² g⁻¹ and a pore volume of 0.21 cm³ g⁻¹.

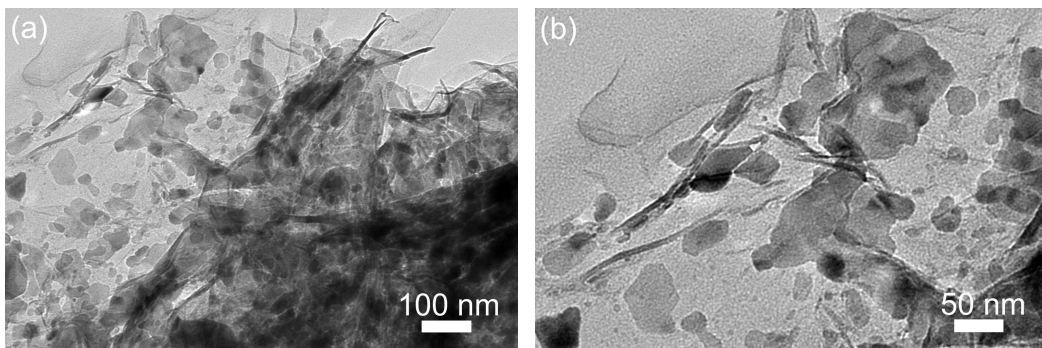


Fig. S10. TEM images of Fe₃O₄/GNS composite.

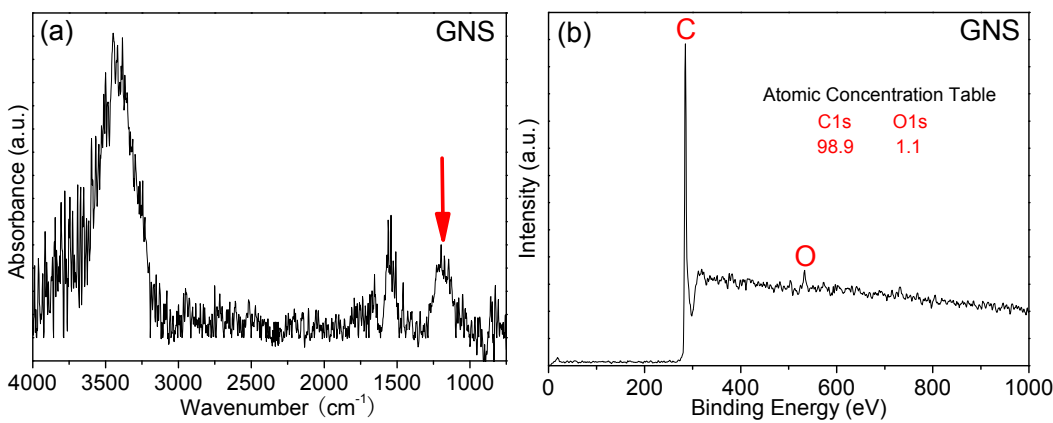


Fig. S11. (a) FT-IR spectrum of GNS. The broad peak from 960 to 1320 cm⁻¹ (red arrow) was due to the C-O bonds on the surface of GNS^[1]; (b) XPS survey spectrum of GNS.

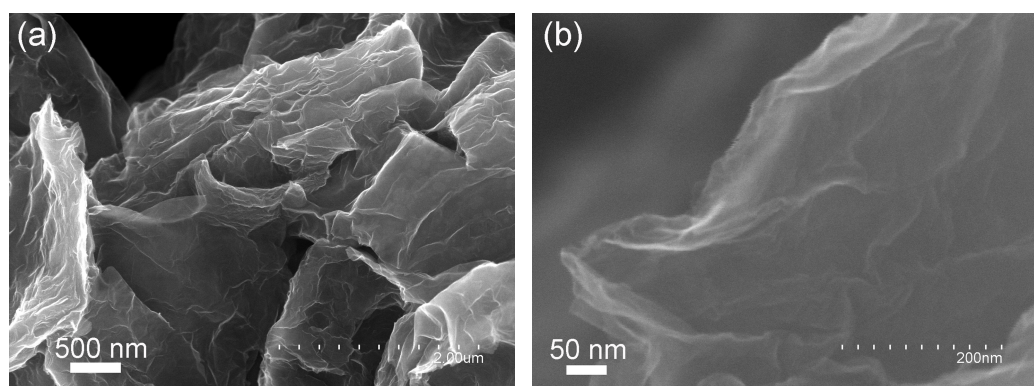


Fig. S12. SEM images of $\text{Fe}(\text{NO}_3)_3 \cdot 9\text{H}_2\text{O}/\text{GNS}$. The GNS was coated by $\text{Fe}(\text{NO}_3)_3 \cdot 9\text{H}_2\text{O}$.

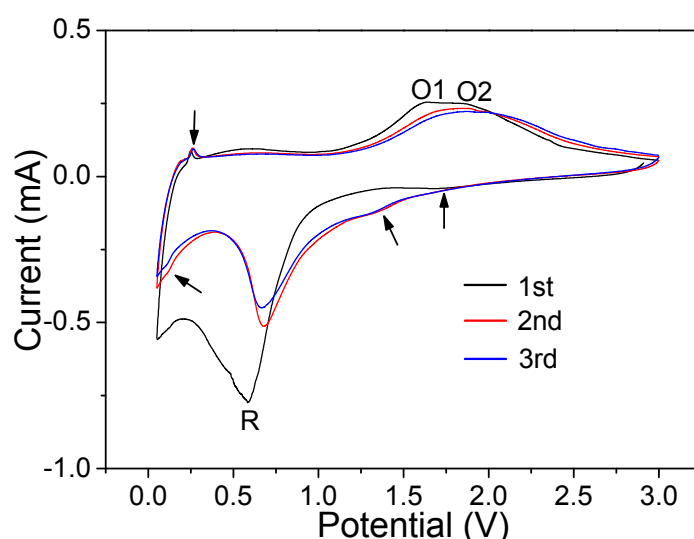


Fig. S13. Cyclic voltammetry curves of the cell with anode prepared from MIO/GNS (scanning rate: 0.2 mV s^{-1} ; scanning range: $0.01\text{--}3.0 \text{ V}$).

The broad peak at $\sim 1.75 \text{ V}$ in the cathodic sweep for the first cycle can be attributed to the formation of $\text{Li}_x\text{Fe}_2\text{O}_3$ intermediates due to lithium insertion.^[2] This peak shifted to $\sim 1.35 \text{ V}$ in the two subsequent cycles possibly due to the formation of different $\text{Li}_x\text{Fe}_2\text{O}_3$.^[3] The strong peak at $\sim 0.59 \text{ V}$ in the cathodic sweep for the first cycle corresponds to the complete reduction of iron and formation of Li_2O . This reduction peak shifted to $\sim 0.67 \text{ V}$ in the subsequent two cycles due to electrode polarization. The peak intensity decreases obviously in the two subsequent cycles, indicating irreversible phase transformation during lithium insertion and extraction in the initial cycle. On the other hand, two broad overlapping peaks at about 1.65 and 1.85 V in the anodic sweep correspond to the oxidation of Fe^0 to Fe^{2+} and further oxidization to Fe^{3+} . There are also two very small peaks, i.e., at $\sim 0.1 \text{ V}$ in the cathodic sweep and $\sim 0.25 \text{ V}$ in the anodic sweep. These two peaks represented the insertion and extraction of lithium ions from the multilayer-stacked graphene, respectively.^[4,5] These electrochemical properties are similar to those of graphite.

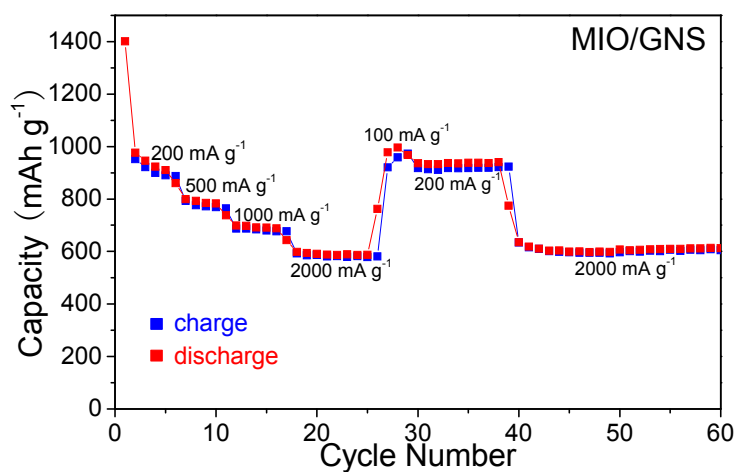


Fig. S14. Capacity retention of MIO/GNS at various current densities.

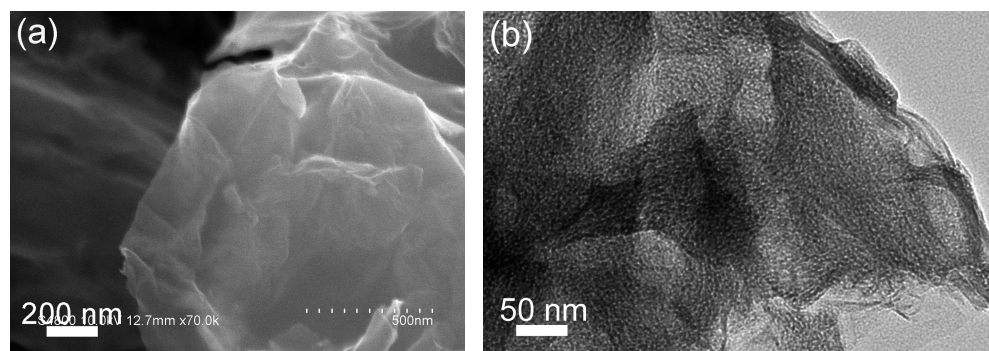


Fig. S15. SEM and TEM images of MIO/GNS nanocomposite with a MIO content of 75 wt%

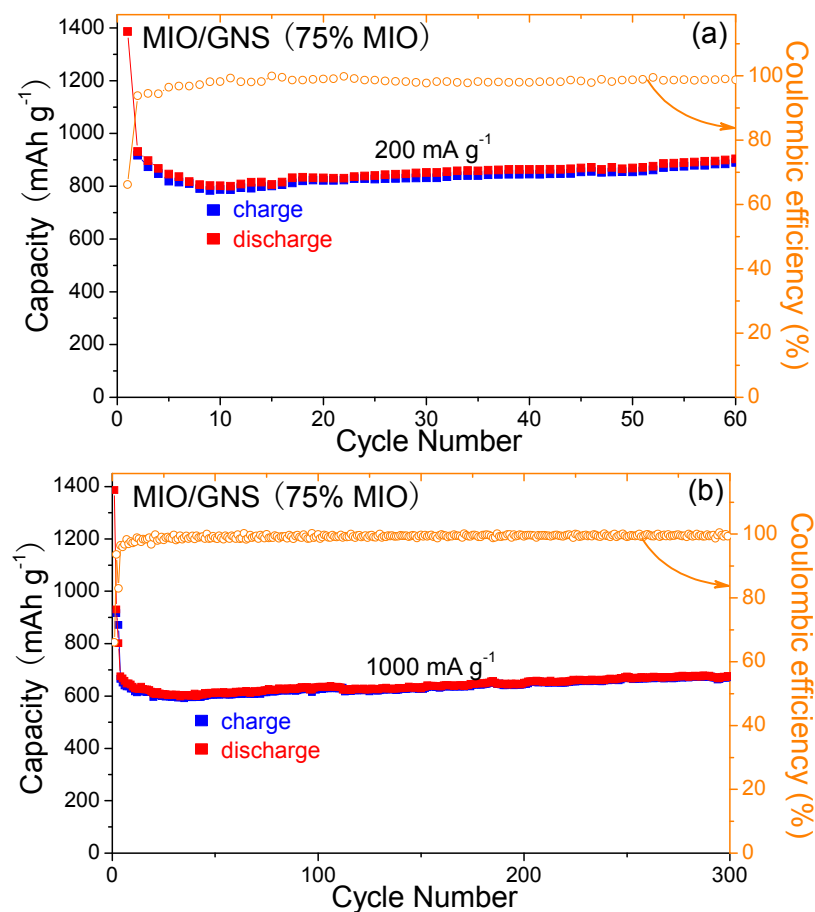


Fig. S16. Capacity retention and Coulombic efficiency of MIO/GNS with a MIO content of 75 wt% at (a) 200 mA g^{-1} and (b) 1000 mA g^{-1} . For the long-term cyclic performance at 1000 mA g^{-1} , the cell was first cycled at a low current density of 200 mA g^{-1} for two cycles.

It is worth noting that the specific capacity of the nanocomposite with 67% MIO (Fig. 4d) is higher than that of the nanocomposite with 75% MIO (Fig. S17b) obtained at the same current density of 1000 mA g^{-1} . The reason is as follows: For the MIO/GNS nanocomposite, a special synergetic effect exists between GNS and MIO nanofilm.^[6,7] The constraint effect of GNS on the volume change of iron oxide can effectively improve the performance of MIO. The presence of MIO nanofilm on the GNS surface effectively prevents the agglomeration of GNS, which is favorable for increasing the Li storage capacity of GNS. Thus, the Li storage capacity of GNS in the nanocomposite is larger than that of simplex GNS.^[6,7] The specific capacity of GNS in the nanocomposite is possibly even larger than that of MIO in the nanocomposite. On the other hand, the rate capability of the composite with 67% MIO is better than that of the composite with 75% MIO because the GNS content for the former is larger than that for the latter. Thus, the specific capacity of the MIO in the former is higher than that in the latter at a large current density. These two reasons result in the higher specific capacity of the nanocomposite with 67% MIO (Fig. 4d) compared with that of the nanocomposite with 75% MIO (Fig. S17b) at the same current density of 1000 mA g^{-1} .

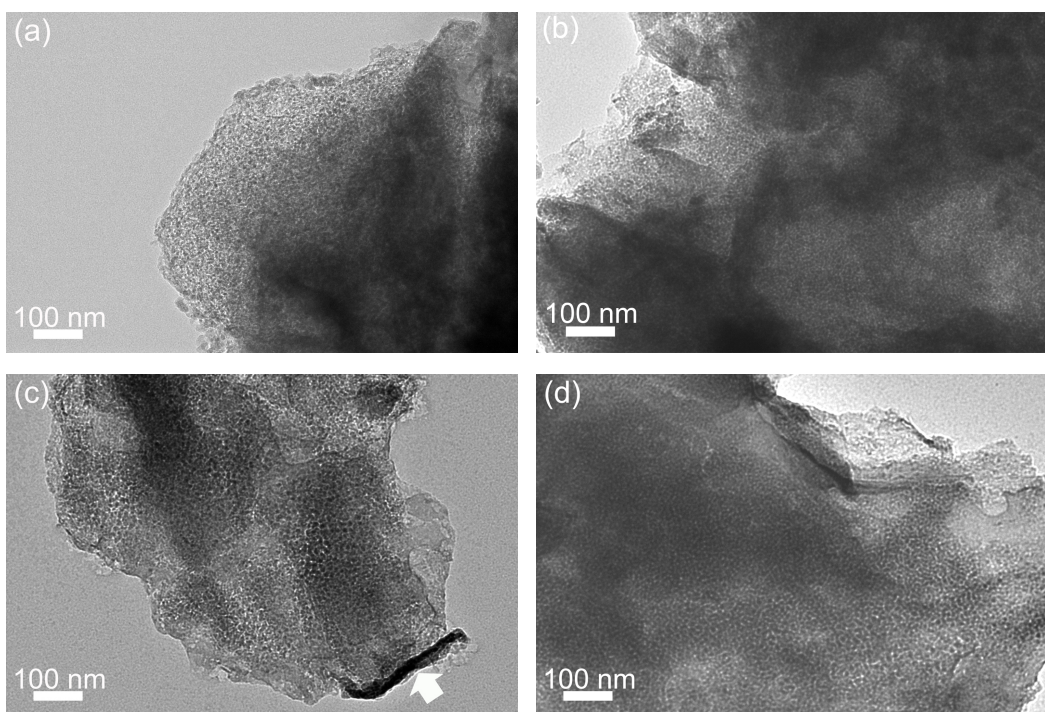


Fig. S17. TEM images of the MIO/GNS (a,b) after 60 discharge/charge cycles at 100 mA g⁻¹ and (c,d) after 400 discharge/charge cycles at 1000 mA g⁻¹. The strong combination of MIO and GNS after 400 cycles can be more directly observed via the side image of the MIO/GNS nanosheet (area marked by an arrow in the lower right corner of (c)).

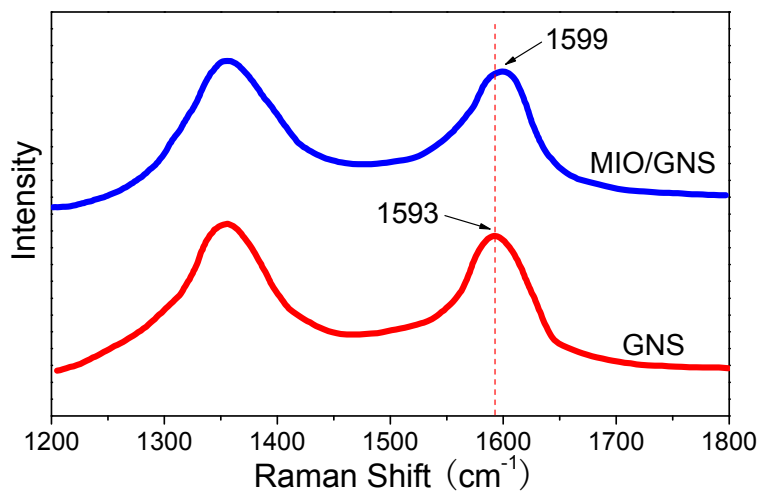


Fig. S18. Raman spectra of GNS and MIO/GNS. The G band shift from 1593 (GNS) to 1599 cm⁻¹ (MIO/GNS) indicates the presence of a charge transfer from graphene to iron oxide, which proves the bond formation between graphene and iron oxide.^[8,9]

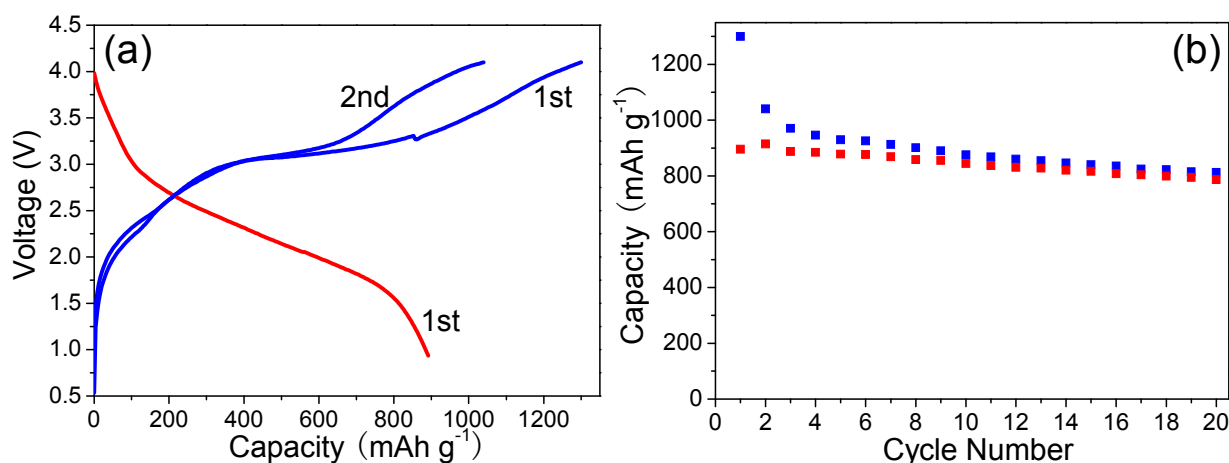


Fig. S19. (a) Discharge and charge curves of the nanocomposite/LiCoO₂ full cell for the first and second cycles at a rate of C/3. (b) Cyclic performance of the full cell. The specific capacity is calculated based on the mass of MIO/GNS nanocomposites.

Reference

- [1] J. Geng, L. Liu, S. B. Yang, S.-C. Youn, D. W. Kim, J.-S. Lee, J.-K. Choi, H.-T. Jung, *J. Phys. Chem. C* **2010**, *114*, 14433.
- [2] B. Sun, J. Horvat, H. S. Kim, W.-S. Kim, J. Ahn, G. Wang, *J. Phys. Chem. C* **2010**, *114*, 18753.
- [3] T. Yoon, C. Chae, Y.-K. Sun, X. Zhao, H. H. Kung, J. K. Lee, *J. Mater. Chem.* **2011**, *21*, 17325.
- [4] P. Guo, G. Zhu, H. Song, X. Chen, S. Zhang, *Phys. Chem. Chem. Phys.* **2011**, *13*, 17818.
- [5] X. Xiao, P. Liu, J. S. Wang, M. W. Verbrugge, M. P. Balogh, *Electrochim. Commun.* **2011**, *13*, 209.
- [6] Z.-S. Wu, W. Ren, L. Wen, L. Gao, J. Zhao, Z. Chen, G. Zhou, F. Li, H.-M. Cheng, *ACS nano* **2010**, *4*, 3187.
- [7] L. Ji, Z. Lin, M. Alcoutlabi, X. Zhang, *Energy Environ. Sci.* **2011**, *4*, 2682.
- [8] J. Zhou, H. Song, L. Ma and X. Chen, *RSC Adv.*, **2011**, *1*, 782.
- [9] G. Zhou, D.-W. Wang, L.-C. Yin, N. Li, F. Li and H.-M. Cheng, *ACS nano*, **2012**, *6*, 3214.